Resolving optical illumination distributions along an axially symmetric photodetecting fiber

Fabien Sorin,[1,2,5] Guillaume Lestoquoy,[2,5] Sylvain Danto,[2] John D. Joannopoulos,[3,4] and Yoel Fink[1,2,3,*]

[1]Department of Materials Science and Engineering, Massachusetts Institute of Technology, 77 Massachusetts Avenue, Cambridge MA 02139, USA
[2]Research Laboratory of Electronics, Massachusetts Institute of Technology, 77 Massachusetts Avenue, Cambridge MA 02139, USA
[3]Institute for Soldier Nanotechnology, Massachusetts Institute of Technology, 77 Massachusetts Avenue, Cambridge MA 02139, USA
[4]Department of Physics, Massachusetts Institute of Technology, 77 Massachusetts Avenue, Cambridge MA 02139, USA
[5]These authors participated equally to this work
*yoel@mit.edu

Abstract: Photodetecting fibers of arbitrary length with internal metal, semiconductor and insulator domains have recently been demonstrated. These semiconductor devices exhibit a continuous translational symmetry which presents challenges to the extraction of spatially resolved information. Here, we overcome this seemingly fundamental limitation and achieve the detection and spatial localization of a single incident optical beam at sub-centimeter resolution, along a one-meter fiber section. Using an approach that breaks the axial symmetry through the constuction of a convex electrical potential along the fiber axis, we demonstrate the full reconstruction of an arbitrary rectangular optical wave profile. Finally, the localization of up to three points of illumination simultaneously incident on a photodetecting fiber is achieved.

OCIS codes: (160.2290) Fiber materials; (040.5160) Photodetectors.

References and links

1. F. Yu, and S. Yin, *Fiber Optic Sensors*, (Marcel-Dekker, 2008).
2. K. T. V. Grattan, and B. T. Meggitt, eds., *Optical Fiber Sensor Technology, Fundamentals*, (Kluwer Academic Publishers, Boston, 2000).
3. A. Rogers, "Distributed optical-fiber sensing," Meas. Sci. Technol. **10**(8), 201 (1999).
4. A. Othonos, and K. Kalli, *Fiber Bragg Gratings—Fundamentals and Applications in Telecommunications and Sensing*, (Artech House, Boston, 1999).
5. M. K. Barnoski, and S. M. Jensen, "Fiber waveguides: a novel technique for investigating attenuation characteristics," Appl. Opt. **15**(9), 2112–2115 (1976).
6. A. J. Rogers, "Polarization-optical time domain reflectometry: a technique for the measurement of field distributions," Appl. Opt. **20**(6), 1060–1074 (1981).
7. A. H. Hartog, "A distributed temperature sensor based on liquid-core optical fibers," J. Lightwave Technol. **1**(3), 498–509 (1983).
8. J. P. Dakin, D. J. Pratt, G. W. Bibby, and J. N. Ross, "Distributed optical fiber raman temperature sensor using a semiconductor light source and detector," Electron. Lett. **21**(13), 569 (1985).
9. T. Kurashima, T. Horiguchi, and M. Tateda, "Distributed-temperature sensing using stimulated Brillouin scattering in optical silica fibers," Opt. Lett. **15**(18), 1038–1040 (1990).
10. C. I. Merzbacher, A. D. Kersey, and E. J. Friebele, "Fiber optic sensors in concrete structures: a review," Smart Mater. Struct. **5**(2), 196–208 (1996).
11. X. Bao, D. J. Webb, and D. A. Jackson, "Combined distributed temperature and strain sensor based on Brillouin loss in an optical fiber," Opt. Lett. **19**(2), 141 (1994).
12. P. J. A. Sazio, A. Amezcua-Correa, C. E. Finlayson, J. R. Hayes, T. J. Scheidemantel, N. F. Baril, B. R. Jackson, D. J. Won, F. Zhang, E. R. Margine, V. Gopalan, V. H. Crespi, and J. V. Badding, "Microstructured optical fibers as high-pressure microfluidic reactors," Science **311**(5767), 1583–1586 (2006).

13. T. T. Larsen, A. Bjarklev, D. S. Hermann, and J. Broeng, "Optical devices based on liquid crystal photonic bandgap fibres," Opt. Express **11**(20), 2589–2596 (2003).
14. B. O'Connor, K. H. An, Y. Zhao, K. P. Pipe, and M. Shtein, "Fiber Shaped Organic Light Emitting Device," Adv. Mater. **19**(22), 3897–3900 (2007).
15. B. O'Connor, K. P. Pipe, and M. Shtein, "Fiber based organic photovoltaic devices," Appl. Phys. Lett. **92**(19), 193306 (2008).
16. M. Fokine, L. E. Nilsson, A. Claesson, D. Berlemont, L. Kjellberg, L. Krummenacher, and W. Margulis, "Integrated fiber Mach-Zehnder interferometer for electro-optic switching," Opt. Lett. **27**(18), 1643–1645 (2002).
17. M. A. Schmidt, L. N. Prill Sempere, H. K. Tyagi, C. G. Poulton, and P. St, "J. Russell, "Wave guiding and plasmon resonances in two-dimensional photonic lattices of gold and silver nanowires," Phys. Rev. B **77**(3), 033417 (2008).
18. H. K. Tyagi, M. A. Schmidt, L. Prill Sempere, and P. S. Russell, "Optical properties of photonic crystal fiber with integral micron-sized Ge wire," Opt. Express **16**(22), 17227–17236 (2008).
19. M. Bayindir, F. Sorin, A. F. Abouraddy, J. Viens, S. D. Hart, J. D. Joannopoulos, and Y. Fink, "Metal-insulator-semiconductor optoelectronic fibres," Nature **431**(7010), 826–829 (2004).
20. A. F. Abouraddy, M. Bayindir, G. Benoit, S. D. Hart, K. Kuriki, N. Orf, O. Shapira, F. Sorin, B. Temelkuran, and Y. Fink, "Towards multimaterial multifunctional fibres that see, hear, sense and communicate," Nat. Mater. **6**(5), 336–347 (2007).
21. M. Bayindir, A. F. Abouraddy, O. Shapira, J. Viens, D. Saygin-Hinczewski, F. Sorin, J. Arnold, J. D. Joannopoulos, and Y. Fink, "Kilometer-long ordered nanophotonic devices by preform-to-fiber fabrication," IEEE J. Sel. Top. Quantum Electron. **12**(6), 1202–1213 (2006).
22. F. Sorin, A. F. Abouraddy, N. Orf, O. Shapira, J. Viens, J. Arnold, J. D. Joannopoulos, and Y. Fink, "Multimaterial Photodetecting Fibers: a Geometric and Structural Study," Adv. Mater. **19**(22), 3872–3877 (2007).
23. A. F. Abouraddy, O. Shapira, M. Bayindir, J. Arnold, F. Sorin, D. S. Hinczewski, J. D. Joannopoulos, and Y. Fink, "Large-scale optical-field measurements with geometric fibre constructs," Nat. Mater. **5**(7), 532–536 (2006).
24. F. Sorin, O. Shapira, A. F. Abouraddy, M. Spencer, N. D. Orf1, J. D. Joannopoulos, and Y. Fink, "Exploiting the collective effects of optoelectronic devices integrated in a single fiber," Nano Lett. **9**(7), 2630–2635 (2009).
25. S. Egusa, Z. Wang, N. Chocat, Z. M. Ruff, A. M. Stolyarov, D. Shemuly, F. Sorin, P. T. Rakich, J. D. Joannopoulos, and Y. Fink, "Multimaterial piezoelectric fibres," Nat. Mater. **9**(8), 643–648 (2010).
26. M. Bayindir, O. Shapira, D. Saygin-Hinczewski, J. Viens, A. F. Abouraddy, J. D. Joannopoulos, and Y. Fink, "Integrated fibers for self-monitored optical transport," Nat. Mater. **4**(11), 820–825 (2005).
27. M. Bayindir, A. F. Abouraddy, J. Arnold, J. D. Joannopoulos, and Y. Fink, "Thermal-Sensing Fiber Devices by Multimaterial Codrawing," Adv. Mater. **18**, 845 (2006).
28. E. K. Sichel, J. I. Gittleman, and P. Sheng, "Electrical properties of Carbon-polymer composite," J. Electron. Mater. **11**(4), 699–747 (1982).
29. N. Orf, O. Shapira, F. Sorin, S. Danto, M. A. Baldo, J. D. Joannopoulos, and Y. Fink, "Multimaterial Fiber Diodes via in situ Compound Synthesis," (manuscript under review).
30. E. Rosencher, and B. Vinter, *Optoelectronics*, (Cambridge University Press, New York, 2002).
31. S. M. Sze, *Semiconductor Devices: Physics and* Technology, 2nd ed. (John Wiley, New York, 2001).
32. R. H. Kingston, *Detection of Optical and Infrared Radiation,* (Springer-Verlag, Berlin, New York, 1978).
33. Z. U. Borisova, *Glassy Semiconductors*, (Plenum Press, New York,1981).
34. S. Danto, F. Sorin, N. D. Orf, Z. Wang, S. A. Speakman, J. D. Joannopoulos, and Y. Fink, "Fiber field-effect device via in situ channel crystallization," Adv. Mater. **22**(37), 4162–4166 (2010).
35. D. S. Deng, N. D. Orf, A. F. Abouraddy, A. M. Stolyarov, J. D. Joannopoulos, H. A. Stone, and Y. Fink, "In-fiber semiconductor filament arrays," Nano Lett. **8**(12), 4265–4269 (2008).

1. Introduction

Optical fibers rely on translational axial symmetry to enable long distance transmission. Their utility as a distributed sensing medium [1–3] relies on axial symmetry breaking either through the introduction of an apriori axial perturbation in the form of a bragg gratings [4], or through the use of optical time (or frequency) domain reflectometry techniques [5,6] which measures scattering from an adhoc axial inhomogeneitie induced by the incident excitation. These have enabled the identification and localization of small fluctuations of various stimuli such as temperature [7–9] and stress [10,11] along the fiber axis. Due to the inert properties of the silica material, most excitations that could be detected were the ones that led to structural changes, importantly excluding the detection of radiation at optical frequencies. Recently, a variety of approaches have been employed, aimed at incorporating a broader range of materials into fibers [12–20]. In particular, multimaterial fibers with metallic and

semiconductor domains have presented the possibility of increasing the number of detectable excitations to photons and phonons [19–25], over unprecedented length and surface area. Several applications have been proposed for these fiber devices in imaging [23,24], industrial monitoring [26,27], remote sensing and functional fabrics [20,21].

So far however, the challenges associated with resolving the intensity distribution of optical excitations along the fiber axis have not been addressed. Here we propose an approach that allows extraction of axially resolved information in a fiber that is uniform along its length without necessitating fast electonics or complex detection architectures. We initially establish the axial detection principle by fabricating the simplest geometry that supports a convex potential profile designed to break the fiber's axial symmetry. Then, an optimal structure which involves a hybrid solid-core/thin-film cross-sectional design is introduced that allows to impose and vary convex electrical potential along a thin-film photodetecting fiber. We demonstrate the localization of a point of illumination along a one-meter photodetecting fiber axis with a sub-centimeter resolution. Moreover, we show how the width of the incoming beam and the generated photoconductivity can also be extracted. Finally, we demonstrate the spatial resolution of three simultaneously incident beams under given constraints.

2. Principle of our approach

Photodetecting fibers typically comprise a semiconducting chalcogenide glass contacted by metallic electrodes and surrounded by a polymer matrix [19–21]. These materials are assembled at the preform level and subsequently thermally drawn into uniform functional fibers of potentially hundreds of meters in length, as illustrated in Fig. 1(A1). An electric potential $V(z)$ across the semiconductor can be imposed along the fiber length by applying a potential drop V_0 at one end as depicted in Fig. 1(A2). As a result, a linear current density j_{dark} is generated in the semiconductor in the dark, between the electrodes. When an incoming optical wave front with an arbitrary photon flux distribution $\Phi_0(z)$ is incident on a fiber of total length L, the conductivity is locally changed and a photo-current (total current measured minus the dark current) is generated due to the photoconducting effect in semiconductors, as illustrated in Fig. 1(A2). The measured photo-current in the external circuitry is the sum of the generated current density $j_{ph}(z)$ along the entire fiber length: $i_{ph} = C \int_0^L V(z)\sigma_{ph}(z)dz$, where C depends on the materials and geometry and is uniform along the fiber axis, and σ_{ph} is the locally generated film photo-conductivity that depends linearly on $\Phi_0(z)$ in the linear regime considered [22–24,30–32]. Note that for simplicity the integrations on the other cylindrical coordinates r and θ are not represented. Also, we neglect the diffusion of generated free carriers along the fiber axis since it occurs over the order of a micrometer, several orders of magnitude lower than the expected resolution (millimeter range).

For the photodetecting fibers considered so far, the conductivity of the semiconductor in the dark and under illmination has been orders of magnitude lower than the one of the metallic electrodes. These electrodes could hence be considered equipotential, and $V(z) = V_0$ along the fiber axis over extend lengths. As a result, j_{dark} is also uniform as depicted on the graph in Fig. 1(A2). Moreover, the photo-current measured in the external circuitry integrates the photo-conductivity distribution $\sigma_{ph}(z)$ along the fiber length. This single, global current measurement does not contain any local information about the incident optical intensity distribution along the fiber axis. In particular, even the axial position of a single incoming optical beam could not be reconstructed. To alleviate this limitation, we propose an approach that breaks the axial symmetry of this fiber system and enables to impose various non-uniform electric potential distributions along the fiber axis. By doing so, we can generate
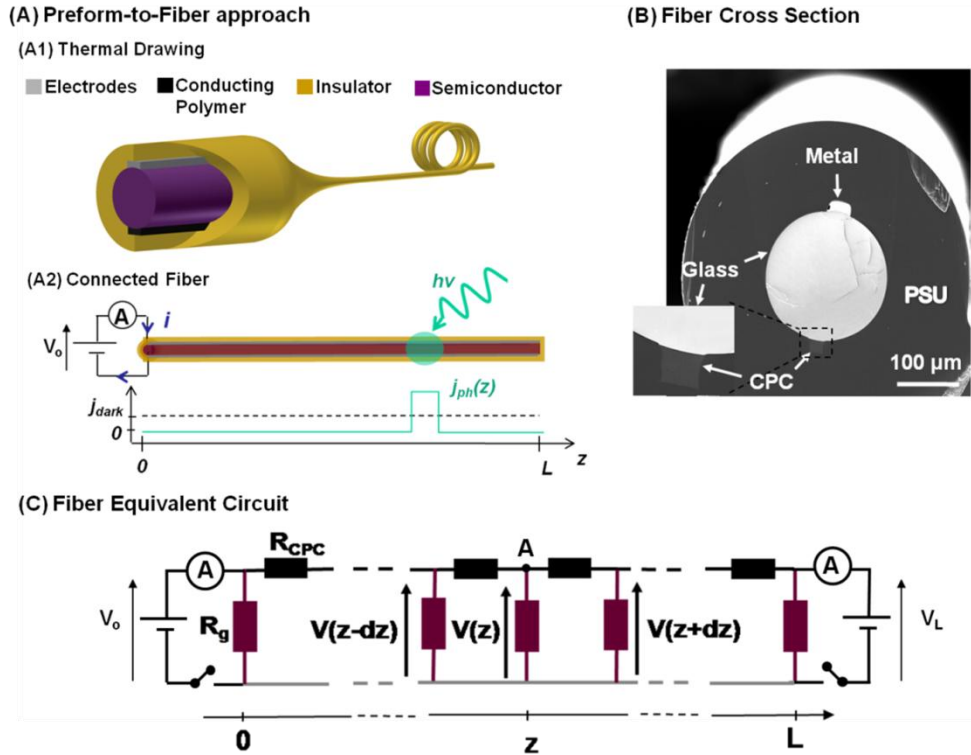
Fig. 1. A(1). 3D Schematic of the multimaterial fiber thermal drawing fabrication approach. A(2). Schematic of a connected photodetecting fiber with an illumination event. The graph represents the linear current density in the dark and under the represented illumination. B. Scanning Electron Microscope micrograph of the fiber cross-section (inset: zoom-in on the contact between the core and the CPC electrode); C. Schematic of the fiber system's equivalent circuit.

and measure several global photo-currents i_{ph} where the fixed and unknown distribution $\sigma_{ph}(z)$ is modulated by different known voltage distributions $V(z)$. We will then be able to access several independent photo-current measurements from which information about the intensity distribution along the fiber axis will be extracted, as we will see.

To controllably impose a non-uniform electrical potential profile $V(z)$, we propose to replace one (or both) metallic conducts by a composite material that has a higher electrical resistivity. This electrode, or resistive channel, can no longer be considered equipotential and the potential drop accors the semiconductor will vary along the fiber axis. An ideal material for this resistive channel was found to be a composite polymer recently successfully drawn inside multimaterial fibers [25], that embeds Carbon black nanoparticles inside a Polycarbonate matrix (hereafter: conducting polycarbonate or CPC) [28]. The CPC resistivity, ρ_{CPC} (1-10 $\Omega.m$ as measured post-drawing), lies in-between the low resistivity of metallic elements (typically 10^{-7} $\Omega.m$) and the high resistivity of chalcogenide glasses (typically 10^6-10^{12} $\Omega.m$) used in multimaterial fibers. It is very weakly dependant on the optical radiations considered so that it will not interfere with the detection process.

To validate this approach we first demonstrate the drawing compatibility of these materials. We fabricated a photodetecting fiber with a semiconducting chalcogenide glass core (of composition $As_{40}Se_{50}Te_{10}$) contacted by one metallic electrode ($Sn_{63}Pb_{37}$) and by another conduct made out of the proposed CPC composite. A Scanning Electron Microscope (SEM) micrograph of the resulting fiber cross-section is shown in Fig. 1B that demonstrate the excellent cross-sectional features obtained. To first theoretically analyze this new system,

we depict its equivalent circuit in Fig. 1C. The semiconducting core can be modelled as multiple resistors in parallel, while the CPC channel is comprised of resistors in series. To find the voltage distribution $V(z)$ in this circuit, we can apply Kirchoff's laws at point A:

$$\frac{V(z)-V(z-dz)}{R_{CPC}} = \frac{V(z+dz)-V(z)}{R_{CPC}} - \frac{V(z)}{R_g}, \quad \text{or} \quad \frac{\partial^2 V}{\partial z^2} = \frac{R_{CPC}}{R_g dz^2}V(z) \qquad (1)$$

or simply:

$$\frac{\partial^2 V}{\partial z^2} = \frac{V(z)}{\delta(z)^2} \qquad (2)$$

with

$$\delta(z) = \sqrt{\frac{\rho_g(z)}{\rho_{cpc}}\frac{\pi}{2}S_{cpc}} \qquad (3)$$

where R_{CPC} is the resistance of the CPC channel over an infinitesimal distance dz ($R_{CPC} = \rho_{CPC}dz/S_{CPC}$), S_{CPC} being the surface area of the CPC electrode in the fiber cross-section. Similarly, R_g is the resistance of a slab of cylindrical semiconducting core of length dz that can be derived by considering a point contact between the electrodes and the solid-core, ($R_g(z) = \pi\rho_g(z)/(2dz)$, with ρ_g the glass resistivity). The new parameter δ has the dimensionality of a length and is referred to as the characteristic length of the fiber system. It can be tuned by engineering the glass composition (hence changing ρ_g), as well as the structure and geometry of the fiber.
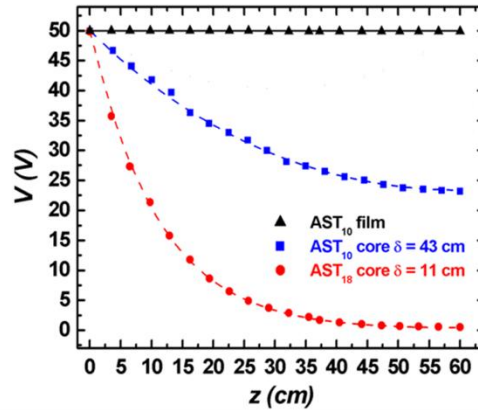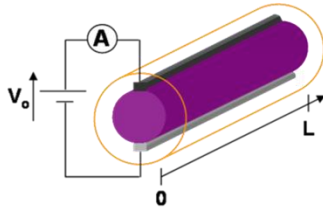
Two sets of boundary conditions depicted in Fig. 2 can be defined for this system: BC(1) where one fiber end ($z = 0$ or L) is brought to a potential $V^{BC(1)}(0) = V_0$ while the other ($z = L$ or 0) is left floating, resulting in $\partial V^{BC(1)}(L)/\partial z = 0$ since no accumulation of charges is expected; and BC(2) where we apply a voltage at both fiber ends, $V^{BC(2)}(0) = V_0$ and $V^{BC(2)}(L) = V_L$. The two potential profiles can then be derived when δ is independent of z, and are given by two *convex* functions:

$$V^{BC1}(z) = \frac{V_0 \cosh\left(\frac{L-z}{\delta}\right)}{\cosh\left(\frac{L}{\delta}\right)} \qquad (4)$$

$$V^{BC2}(z) = \frac{V_0 \sinh h\left(\frac{L-z}{\delta}\right) + V_L \sinh h\left(\frac{z}{\delta}\right)}{\sinh\left(\frac{L}{\delta}\right)} \qquad (5)$$

To assess our model, we fabricated three fibers with different materials and structures. All fibers have one metallic electrode ($Sn_{63}Pb_{37}$ alloy) and one CPC electrode of same size. Two fibers have a solid-core structure like the one shown in Fig. 1B, with two different glass compositions from the chalcogenide system As-Se-Te, $As_{40}Se_{50}Te_{10}$ (AST_{10}) and $As_{40}Se_{42}Te_{18}$ (AST_{18}). The third fiber has a thin-film structure with a 500 nm layer of $As_{40}Se_{50}Te_{10}$ [22,24]. This thin film structure is expected to have a very large characteristic length since its conductance is many orders-of-magnitude lower than the one of both metallic and CPC electrodes. In solid-core fibers however, δ should be of the order of the fiber length, inducing a significant variation in the potential profile.

(A) Boundary condition 1 (BC1)
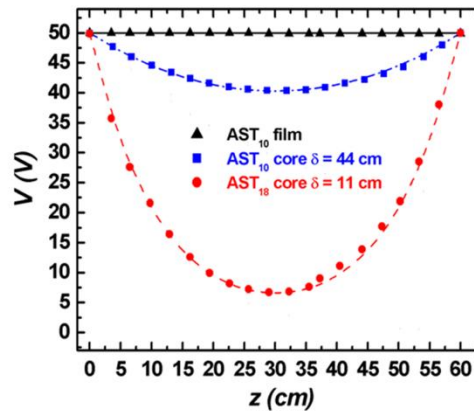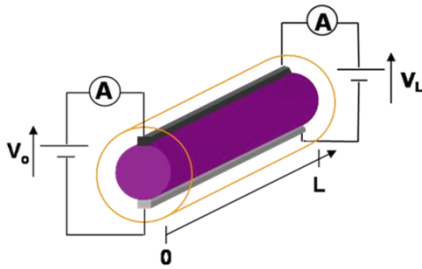

(B) Boundary condition 2 (BC2)

Fig. 2. (A) Schematic of the fiber contact for boundary conditions (1) and graph representing the experimental results (dots) and the fitted theoretical model (lines) of the voltage profile between the CPC electrode and the metallic conduct at different points along the fiber axis, when the fiber is under BC(1) and for different fibers: in black, AST_{10} thin-film; in blue, AST_{10} core and in red, AST_{18}. (B) Same as (A) but when the fiber is under BC(2).

Separate measurement of the CPC electrode resistiviy ($\rho_{CPC} = 1.4 \ \Omega.m$ and $\rho_{CPC} = 1.2 \ \Omega.m$ in pieces from the AST_{10} and AST_{18} fibers respectively) and the glass conductivities lead to expected δ values of 40 cm and 9 cm in the AST_{10} and AST_{18} fibers respectively, the higher conductivity of AST_{18} being responsible for the lower δ parameter [33].

We then cut a 60-cm-long piece from each fiber and made several points of contact on the CPC electrodes while contacting the metallic conduct at a single location. We applied a 50 V potential difference for both BC(1) and BC(2), and measured the potential drop between the contact points along the CPC channel and the equipotential metallic conduct, using a Keithley 6517A multimeter. The experiment was performed in the dark to ensure the uniformity of δ. The results are presented in Fig. 2 where the data points are the experimental measurements while the curves represent the theoretical model derived above, fitted over δ. As we expected, the thin-film fiber maintains a uniform potential along its axis. For solid-core fibers, the fitting values (43 cm and 11 cm for BC(1), and 44 cm and 11 cm for BC(2) for AST_{10} and AST_{18} fibers respectively) match very well with the expected δ parameters given above. The discrepancy is due to errors in measuring the different dimensions in the fiber, and potential slight non-uniformity of the glass conductivity due to local parasitic crystallization during the

fabrication process [34]. Noticeably, the δ values obtained for both boundary conditions are in excellent agreement, which strongly validates our model.

3. Hybrid Thin-film/Solid-core fiber structure

Solid core fibers can hence support convex potential profiles that can be tuned using different glass compositions or fiber structure. When an optical signal is impingent on the fiber however, δ is no longer uniform as we considered earlier, since the glass resistivity is locally changed. This will in turn affect $V(z)$ that becomes an unknown function of the intensity distribution of the optical wave front. Moreover, thin-film structures are a more attracting system to work with in light of their better sensitivity and other advantages described in ref [22]. To address these observations we propose an hybrid structure that enables to impose convex potential distributions that remain unchanged under illumination, accross a semiconducting thin-film that is used as the higher sensitivity detector. The fiber cross-section is shown in Fig. 3A, where a CPC electrode contacts both a solid-core and a thin-film structure. The equivalent circuit is represented in Fig. 3C, where one can see that the two systems are in parallel. The drop of potential between the CPC channel and the metalic electrodes (both at the same potential) expressed in Eq. (1) now becomes: $V(1/R_c + 1/R_f)$ where R_c and R_f are the resistance of a slab of cylindrical semiconducting solid-core and thin-film respectively, of length dz. This leads to a new differential equation:

$$\frac{\partial^2 V}{\partial z^2} = V \left(\frac{1}{\delta_c^2} + \frac{1}{\delta_f^2} \right) \approx \frac{V}{\delta_c^2} \tag{6}$$

since δ_c and δ_f, the characteristic parameters for the solid-core and the thin-film respectively, verify $\delta_c \ll \delta_f$ as can be anticipated from earlier results. The potential distribution is hence imposed by the solid-core system, while the current flowing through the photoconducting film can be measured independently, thanks to the different metallic electrodes contacting the solid-core and the thin-film structures. Similar boundary conditions can be imposed to the solid-core sub-system as before.

To verify our approach we fabricated a fiber integrating a structure with a CPC electrode in contact with both a solid-core of AST_{10} and a thin layer of the $As_{40}Se_{52}Te_8$ glass. This glass composition was chosen for its better thermal drawing compatibility with the polysulfone (PSU) cladding used here, which results in a better layer uniformity. Note that in this fiber, the metallic electrodes were embedded inside a CPC electrode. The conductivity of this assembly is still dominated by the high conductivity of the metal. The high viscosity of CPC in contact with the thin-film is however beneficial to maintain a layer of uniform thickness [35]. The contacts between the CPC electrodes and the glasses were found to be ohmic.

We reproduced the experiment described above to measure the potential drop between the CPC and the metallic electrodes along a one-meter long fiber piece. This time however, the experiment was done under three conditions: first in the dark, then when the fiber was illuminated, at the same location, by a white light source and then by a green (532 nm) LED, with intensity so that the generated photo-current in the thin-film by both illumination was almost the same. The results are shown in Fig. 3B and illustrate the proposed concept very well. Indeed, Since the green light is almost fully absorbed in the semiconducting layer [24], a significant change of thin-film resistivity (and hence a high photo-curent) can be obtained while leaving δ_c, and thus the potential distribution across the layer, unchanged. White light on the other hand penetrates much deeper in the material and will change the conductivity of both the thin-film and the fiber core, changing δ_c and the voltage distribution. From these
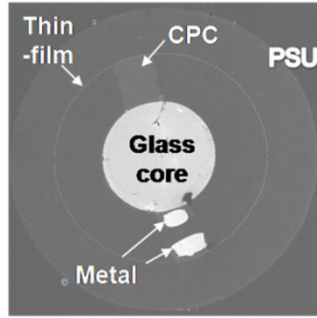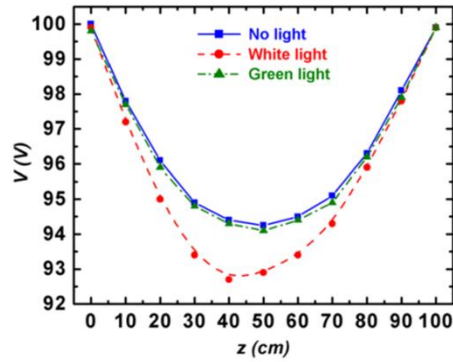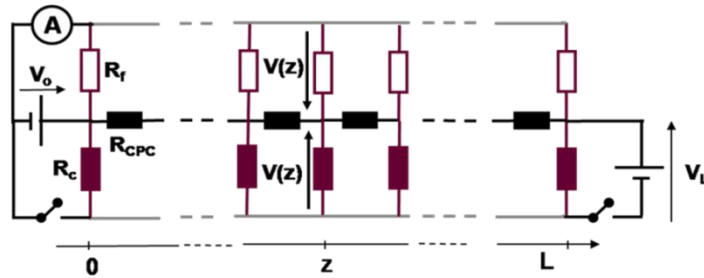
(A) Fiber Cross-section

(B) Voltage Profile

(C) Equivalent Circuit

Fig. 3. A. SEM micrograph of a fiber with the new thin-film/solid-core structure. B. Experimental results (dots, the lines are added for clarity) of the voltage profile of a one-meter long fiber piece from panel A in the dark (in blue), and under a spot of white light (in red) and green light (in green) at the same location, same width and of similar intensity. C. schematic of the electrical connection to one fiber end.

experiments we could extract the value $\delta_c = 143$ cm for this fiber system. This value is much larger than measured before due to the increase of S_{CPC} imposed by the new structure design. Note that we used green versus white light for this proof of concept, but many fiber parameters such as the glass composition or fiber geometry can be tuned to apply this approach to a wide range of radiation frequencies.

Our new fiber system can now support a fixed potential profile $V(z)$ that can be varied by changing the applied boundary conditions. Given the linear relation of hyperbolic functions that appear in the convex potential profiles derived in Eq. (3), one realizes that all possible profiles are a linear combination of the two functions:

$$V^I(z) = \frac{V}{\sinh\left(L/\delta_c\right)}\sinh h\left(\frac{L-z}{\delta}\right) \tag{7}$$

and

$$V^{II}(z) = \frac{V}{\sinh\left(L/\delta_c\right)}\sinh h\left(\frac{z}{\delta}\right) \tag{8}$$

obtained for the boundary conditions $V_0 = V$ and $V_L = 0$, and vice versa. A third independent voltage profile can also be imposed by applying a voltage between the CPC electrode and the electrode contacting the thin-film only, resulting in a nearly uniform potential $V^{III}(z) = V$, since δ_f is much larger than the fiber lengths considered. Hence, we can measure three independent photo-currents that result from the integration of the stimuli intensity profile

modulated by these different voltage distributions, from which some axial information about σ_{ph} and hence Φ_0 can be extracted as we show below.

4. Resolving a single optical beam

Let us consider the case of an incident uniform light beam, with a rectangular optical wave front, at a position z_0 along the fiber axis, and with a width $2\Delta z$. It generates a photo-conductivity profile $\sigma_{ph}(z) = \sigma_{ph}$ if $z \in [z_0 - \Delta z, z_0 + \Delta z]$, and 0 otherwise. The generated current for each configuration can be derived, integrating over the illumination width and re-arranging the hyperbolic terms:

$$i_{ph}^I = \frac{2CV\sigma_{ph}}{\sinh(L/\delta_c)}\sinh h\left(\frac{L-z_0}{\delta_c}\right)\sinh h\left(\frac{\Delta z}{\delta_c}\right) \tag{9}$$

$$i_{ph}^{II} = \frac{2CV\sigma_{ph}}{\sinh(L/\delta_c)}\sinh h\left(\frac{z_0}{\delta_c}\right)\sinh h\left(\frac{\Delta z}{\delta_c}\right) \tag{10}$$

$$i_{ph}^{III} = 2CV\sigma_{ph}\Delta z \tag{11}$$

Remarkably, the first two currents are a function of the beam position which can be simply extracted by taking the ratio $r = i_{ph}^I / i_{ph}^{II}$ leviating the dependence on the beam intensity and width. We can extract z_0 from the measurement of r through the relation:

$$z_0 = \frac{\delta_c}{2}\ln\left[\frac{e^{L/\delta_c}+r}{e^{-L/\delta_c}+r}\right] \tag{12}$$

This was experimentally verified by illuminating a one-meter long piece of the fiber shown in Fig. 3, with a 1 cm width beam from a green LED, at different locations along the fiber length. The results are shown in Fig. 4A where the straight line represents the experimental points of illumination of the fiber while the dots are the reconstructed positions from measuring the ratio of photo-currents r. The agreement between the experimental and measured positions is excellent, with errors made on the position smaller than $\pm$ 0.4 cm in the middle of the fiber.

Fluctuations of the photo-currents come from various sources [30–32] and results in variations of the ratio r and hence in errors in the measured beam's position. The axial resolution of this system depends on a large number of parameters (fiber length, δ_c, beam position and intensity, fiber materials and geometry etc...), and an exhaustive study of it is beyond the scope of this paper. We can however assess the resolution of our system in the experimental conditions of the data shown in Fig. 4A. To do so we first measure the dark current noise i_N, considered in good approximation to be the only source of noise here. We found it to be around 10 pA in our experimental conditions, using similar techniques as those explained in ref [22]. This noise current is the same for configurations I and II given the symmetry of the system. Intuitively, when one measures a photo-current $i_{ph}^{I,II}$, its mean value lies within the segment defined by $i_{ph}^{I,II} \pm i_N$. In a simple and conservative approach, we define the resolution of our system as the difference z_{0+}- z_{0-} of the two obtained positions z_{0+} and z_{0-} when the maximum error on the currents are made, i.e when r is given by
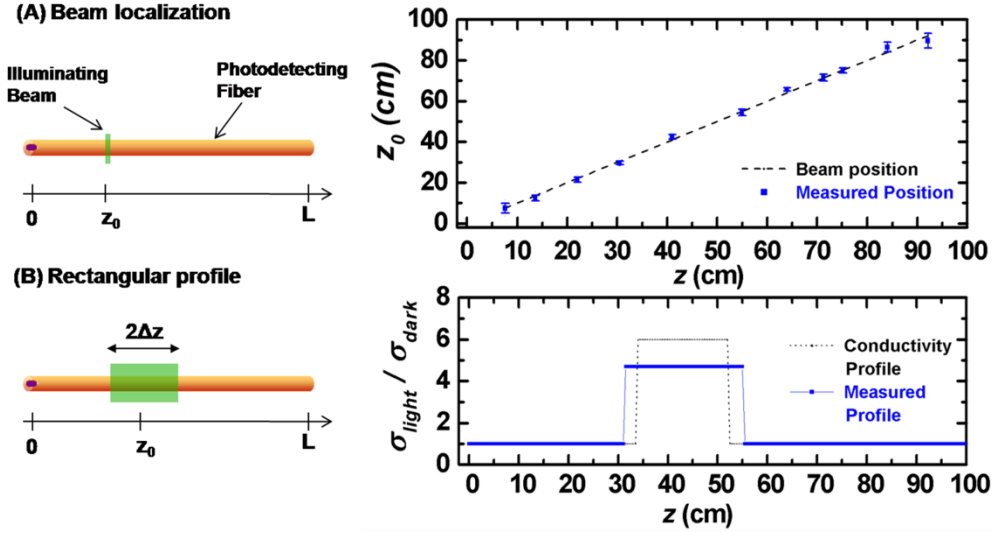
Fig. 4. Schematic of the illuminated fiber by a single optical beam and graph of the real position (black dashed line) and reconstructed position with error bars(blue dots) of an optifcal beam incident on a 1 m-long fiber at different positions. (B) Schematic of the illuminated fiber by a rectangular optical wave front. And graph of the real profile (black doted line) and reconstructed profile (blue dots) of a rectangular wave front incident on the same fiber.

$r_+ = \left(i_{ph}^I + i_N\right)/\left(i_{ph}^{II} - i_N\right)$ and $r_- = \left(i_{ph}^I - i_N\right)/\left(i_{ph}^{II} + i_N\right)$ respectively. These error bars are represented in the graph of Fig. 4A. The resolution found is sub-centimeter, corresponding to two orders of magnitude smaller than the fiber length. Note that the fiber materials and geometry can be tuned using the approaches described in ref [22]. to achieve targeted axial resolution and sensitivity, given the expected stimulus intensity. This is to the best of our knowlegdge the first time that a beam of light can be localized over such an extended length and with such a resolution, using a single one dimensional distributed photodetecting device requiring only four points of electrical contact.

The beam position is not the only spatial information we can reconstruct with this system. Indeed, the ratio of i_{ph}^{II} and i_{ph}^{III} allows us to reconstruct Δz as z_0 is known, by measuring the ratio $\sinh(\Delta z/\delta_c)/(\Delta z/\delta_c)$. This also enables to evaluate σ_{ph}, using i_{ph}^{III}, and hence reconstruct the associated beam intensity . In Fig. 3B we show the experimental illumination profile of a green LED light (black dashed line, centered at 43 cm, width 18 cm, with a conductivity $\sigma_{ph} = 6\,\sigma_{dark}$) and the reconstructed profile from current measurements (blue data points, centered at 43.5 cm, width 24 cm and $\sigma_{ph} = 4.7\sigma_{dark}$). The positioning is very accurate as expected from the results above, while a slightly larger width is measured. This error is due to the large value of δ_c compared to Δz, which results in a ratio of i_{ph}^{II} to i_{ph}^{III} more sensitive to noise than the ratio of i_{ph}^I over i_{ph}^{II}. It is however clear from discussions above that the fiber system can be designed to have a much better resolution for different beam width ranges, by tuning δ_c to smaller values.

Also under study is the integration time required for this system. The speed at which we can vary the potentials depends on the bandwidth associated with the equivalent circuit, taking into account transient current effects in amorphous semiconductors. In this proof-of-concept, measurements were taken under DC voltages applied, varrying the boundary conditions after transient currents are stabilized (typically after a few seconds). Novel designs, especially fibers where the semiconducting material has been crystallized through a post-drawing

crystallization process [34], and integrating rectifying junctions that have proven to have several kHz of bandwidth [29], could result in significant improvement in device performance and speed.

5. Extracting axial information from multiple incoming beams

When more than one beam are incident on the fiber, each one brings a set of three unknown parameters to be resolved (its axial position, width and power). Since our detection scheme provides three independent photo-currents, some prior knowledge on the stimuli is then required to localize each beam along the fiber axis. For example, we can localize two similar illumination events (with approximately same width and power), that are incident at different axial positions. Let us consider the simpler case where two such beams impinging the fiber have a width $2\Delta z$ much smaller than the solid-core characteristic length δ_c (so that $\sinh(\Delta z/\delta_c)/(\Delta z/\delta_c) \approx 1$). They each generate a photo-conductivity σ_{ph} at their positions z_1 and z_2 (with $z_1 < z_2$). The photo-currents measured are the sum of the measured currents with individual beams. Defining $Z_m = \dfrac{z_1 + z_2}{2}$ and $Z_D = \dfrac{z_2 - z_1}{2}$, we can derive:

$$i_{ph}^{I} = \frac{4CV\sigma_{ph}}{\sinh(L/\delta_c)}\sinh h\left(\frac{\Delta z}{\delta_c}\right)\sinh h\left(\frac{L-Z_m}{\delta_c}\right)\sinh h\left(\frac{Z_D}{\delta_c}\right) \tag{13}$$

$$i_{ph}^{II} = \frac{4CV\sigma_{ph}}{\sinh(L/\delta_c)}\sinh h\left(\frac{\Delta z}{\delta_c}\right)\sinh h\left(\frac{Z_m}{\delta_c}\right)\sinh h\left(\frac{Z_D}{\delta_c}\right) \tag{14}$$

$$i_{ph}^{III} = 4CV\sigma_{ph}\Delta z \tag{15}$$

Following the same approach as in the single beam case, we can reconstruct Z_m and Z_D, and hence z_1 and z_2. In Fig. 5A, we show the experimental illumination of a fiber with two identical beams of width 6 cm from the same green LED (dashed black curve) at positions 54 cm and 75 cm. The blue dots represent the reconstructed beams' positions, with measured position 51 ± 3 cm and 78 ± 3 cm for the two beams. The error on the positions were computed in a similar fashion as before.

An optical signal made out of three beams requires even more additional constraints to be resolved. For example, three similar beams equidistant from one to the next can be detected and localized with our system. Indeed, here again only two unknowns have to be found: the central beam position and the distance between two adjacent beams. The derivation of the algorithm to extract these positions from the different current measurements is very similar to what has been derived above. In Fig. 5B we show experimental results of the localization of three incoming beams of same width ($\Delta z = 6$ cm) and intensity (generating a photo-conductivity $\sigma_{ph} = 8.5\sigma_{dark}$) at positions $z_1 = 35.5$ cm, $z_2 = 55.5$ cm, and $z_3 = 75.5$ cm. The generated conductivity pattern is represented by a black doted line on the graph. The reconstructed positions from photo-current measurements were 30 ± 4 cm, 51.5 ± 4 cm and 73 ± 4 cm, in very good agreement with the real beams locations. Note that in these two multiple beams cases, we could only extract the position of the beams but not their intensity nor width. If we knew the width of each beam however, we would be able to extract the position and intensity assuming that this intensity is the same.
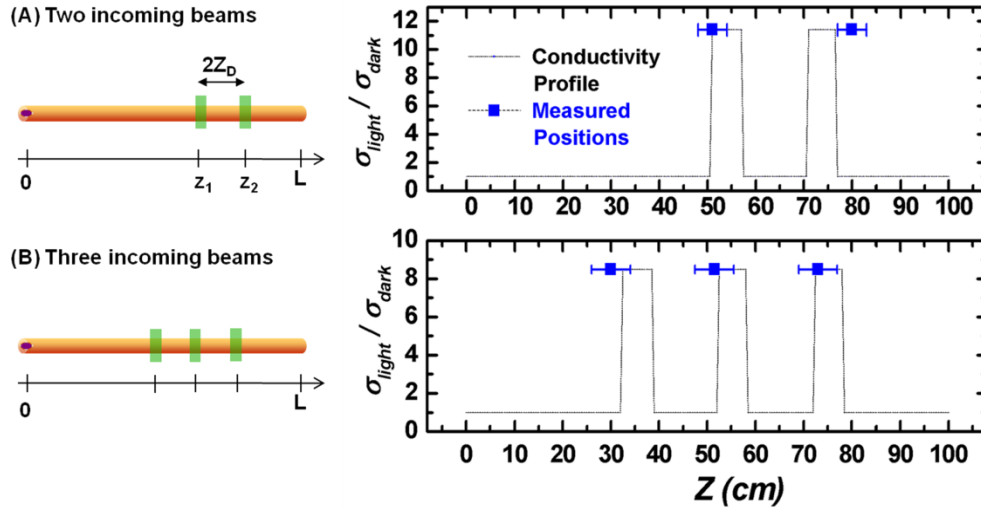
Fig. 5. (A) Schematic: photodetecting fiber illuminated by two similar optical beams. Graph: position measurements of the two beams. In black doted line is the conductivity profile generated by the two incoming beams while the blue dots are the reconstructed positions with the error bars. (B) Schematic: photodetecting fiber illuminated by three similar optical beams. Graph: position measurements of the three beams. In black doted line is the conductivity profile generated by the three incoming beams while the blue dots are the reconstructed positions with the error bars.

6. Conclusion

In conclusion, axially resolved optical detection was achieved in an axially symmetric multimaterial fiber. A fiber architecture that combines insulating and semiconducting domains together with conductive metallic and polymeric materials was demonstrated. This architecture supports a convex electric potential profile along the fiber axis that can be varied by changing the boundary conditions. As a result, the position, width and the intensity of an arbitrary incoming rectangular optical wavefront could be reconstructed. Under given constraints, two and three simultaneously incident beams could also be spatially resolved. The ability to localize stimuli along an extended fiber length using simple electronic measurement approaches and with a small number of electrical connections, presents intruiging opportunities for distributed sensing.

Acknowledgments